Energy & Environmental Science

Understanding the thermally activated charge transport in NaPbmSbQm+2 (Q = S, Se, Te) thermoelectrics: weak dielectric screening leads to grain boundary dominated charge carrier scattering

Journal:	*Energy & Environmental Science*
Manuscript ID	EE-ART-02-2020-000491.R1
Article Type:	Paper
Date Submitted by the Author:	20-Mar-2020
Complete List of Authors:	Slade, Tyler; Northwestern University, Chemistry Grovogui, Jann; Northwestern University, Materials Science and Engineering Kuo, Jimmy; Northwestern University, Department of Materials Science and Engineering Anand, Shashwat; Northwestern University, Materials Science and Engineering Bailey, Trevor; University of Michigan, Department of Physics Wood, Max; Northwestern University, Materials Science and Engineering Uher, Ctirad; University of Michigan, Department of Physics Snyder, G.; Northwestern University, Department of Materials Science and Engineering Dravid, Vinayak; Northwestern University, Materials Science & Engineering Kanatzidis, Mercouri; Northwestern University, Department of Chemistry

SCHOLARONE™
Manuscripts

Understanding the thermally activated charge transport in $NaPb_mSbQ_{m+2}$ (Q = S, Se, Te) thermoelectrics: weak dielectric screening leads to grain boundary dominated charge carrier scattering

Tyler J. Slade,[1] Jann A. Grovogui,[2] Jimmy Jiahong Kuo,[2] Shashwat Anand,[2] Trevor P. Bailey,[3] Maxwell Wood,[2] Ctirad Uher[3], G. Jeffrey Snyder,[2] Vinayak P. Dravid,[2] Mercouri G. Kanatzidis[1*]

[1]Department of Chemistry, Northwestern University, Evanston, Illinois 60208, USA.

[2]Department of Materials Science and Engineering, Northwestern University, Evanston, Illinois 60208, USA.

[3]Department of Physics, University of Michigan, Ann Arbor, Michigan 48109, USA.

Abstract:

Many thermoelectric materials feature irregular electrical conductivity with thermally activated transport below ~600 K and metallic behavior at high temperatures, despite possessing degenerate carrier concentrations. The suppression of the electrical conductivity ultimately degrades the thermoelectric performance on the cold side and limits the device energy conversion efficiency. As such, establishing the origin of the low temperature scattering and developing strategies to mitigate its effect are paramount issues. To date, the correct microscopic description of the low temperature carrier scattering remains an open issue, and there is little work addressing why some thermoelectric materials are more susceptible to the deleterious behavior. Here, we use the promising thermoelectric alloys of PbQ and $NaSbQ_2$ (Q = S, Se, Te) as model systems to address these concerns. We directly show the thermally activated transport stems from the scattering of charge carriers by the grain boundaries (GBs), and that the expected metallic electrical conductivity is recovered by preparing large grained samples with reduced densities of GBs. We furthermore study the electrical properties $NaPb_mSbSe_{m+2}$ as a function of $NaSbSe_2$ fraction, as well as those of the chalcogenide analogues, PbTe–$NaSbTe_2$ and PbS–$NaSbS_2$, and demonstrate that the strength of GB scattering can be understood by utilizing simple chemical principles. By considering the polarizability of the host atoms, we directly relate the magnitude of GB scattering to the relative degree of charge carrier screening in each material, and demonstrate that GB

scattering is strongest in the ionic $NaSbQ_2$–rich compounds and weakest in more polarizable PbQ–rich phases. We finally show how these chemical arguments elegantly explain the strong GB scattering in numerous other thermoelectric materials. By uniting the deleterious charge transport properties exhibited by many different compounds into a common picture, we discuss how our work gives design principles for proper microstructure engineering in emerging thermoelectric materials.

Introduction:

Thermoelectric modules are quiet, reliable, and emission free systems capable of both converting heat into electrical energy and solid-state cooling. As such, thermoelectric technology is attractive for potential applications in waste heat recovery, remote electricity generation, space exploration, and environmentally friendly refrigeration.[1, 2] Indeed, over the past two decades, researchers directed intense efforts toward thermoelectric technology, making significant progress in both the improvement of traditional thermoelectric materials[3-7] and the discovery of new and promising candidates.[8-11] Despite the steady advancement, the high cost and/or low efficiencies of most thermoelectric materials are impediments for thermoelectric technology to achieve widespread utilization, and improving material performance remains a key challenge facing the field. The maximum energy conversion efficiency of a thermoelectric material is parameterized by the dimensionless figure of merit $ZT = \frac{\sigma S^2}{\kappa} T$ where σ is the electrical conductivity, S is the Seebeck coefficient, κ is the thermal conductivity, and T is the absolute temperature. In many of the most common thermoelectric materials ZT is maximized at temperatures greater than 600 K. However, because modules operate across a temperature gradient, maximizing the figure of merit at both hot and cold sides is critical to achieving the best performance.[12]

The demand for large ZT values between low and high temperatures is particularly relevant in many emerging thermoelectric materials that exhibit seemingly anomalous thermally activated

electrical conductivity below ~600 K. Examples include $NaPb_mSbSe_{m+2}$,[13] SnSe,[14] Mg_3Sb_2,[15] $KAlSb_4$,[16] CoSb,[17] NbFeSb,[18] and Ge-alloyed PbSe.[19] An illustration of the temperature-dependent electrical conductivity typical in these materials is shown in Figure 1a. Considering these materials are typically degenerately doped (e.g. charge carrier concentrations greater than $10^{19\text{-}20}$ cm^{-3}) , such semiconducting-like behavior is highly irregular, as phonon scattering is expected to dominate the electrical transport and yield a negative temperature dependence at these doping concentrations.[20] From the standpoint of engineering high quality thermoelectrics, the unusual charge transport behavior is undesirable, as it suppresses the power factor (σS^2) at low temperatures and ultimately degrades the device figure of merit. Establishing a detailed understanding of the mechanism behind the low temperature carrier scattering and developing routes to mitigate its effect are therefore crucial application issues and are furthermore of fundamental interest.

In recent work on Mg_3Sb_2, Kuo *et. al* explained the irregular electrical behavior by proposing that the charge carriers are strongly scattered by energy barriers present at the grain boundaries (GBs).[21] In polycrystalline forms of many traditional semiconductors such as Si, CdSe, and GaAs, energy barriers are known to form at the GBs and restrict electronic conduction.[22-28] Despite this, the impact of the GBs is rarely discussed in the context of charge transport in thermoelectric materials. Drawing on the previous work, Kuo *et al*. proposed that in Mg_3Sb_2, otherwise mobile charge carriers are impeded when encountering the GBs, limiting the electrical conductivity at low temperatures; however, with further heating, an increasing number of electrons or holes are thermally excited across the potential barriers, and the electrical conductivity rises. Eventually, when the temperature is sufficiently high, the expected phonon scattering becomes the dominant scattering mechanism, giving rise to the classic negative temperature dependence of the conductivity. This model shows that the combination of GB dominated transport at low

temperatures and phonon scattering at high temperatures can produce the distinctive σ vs. T curve illustrated in Figure 1a.

While the GB model provides an accurate theoretical account of the otherwise mysterious electrical behavior, it also raises several important questions. Foremost, other models such as ionized impurity scattering can give qualitatively similar temperature dependent behavior and have also been invoked to explain the irregular transport properties.[15, 29] Currently, debate remains on the proper microscopic description of the low–temperature scattering. Furthermore, there is little work addressing why some materials are seemingly more prone to this deleterious behavior than others. For example, both $NaPb_mSbSe_{m+2}$ and $AgPb_mSbSe_{m+2}$ families are reported to exhibit strong charge carrier scattering under ~ 500 K;[13, 30] however, the closely related tellurides $NaPb_mSbTe_{m+2}$ and $AgPb_mSbTe_{m+2}$ behave as typical degenerate semiconductors.[31-33]

Here, we address these issues by studying the unusual charge carrier scattering in alloys of PbSe with $NaSbSe_2$ ($NaPb_mSbSe_{m+2}$) and the chalcogenide analogues $NaPb_mSbS_{m+2}$ and $NaPb_mSbTe_{m+2}$. We first provide unambiguous evidence directly linking the thermally activated conductivity to the grain boundaries. By preparing $NaPb_mSbSe_{m+2}$ samples with identical chemical compositions and varying grain sizes, we show that the low–temperature scattering is suppressed, and the expected metallic behavior is recovered as the density of boundaries is reduced. We next propose simple chemical guidelines for addressing what compounds will be most susceptible to GB limited electrical conductivity. We suggest that GB scattering will be strongest in materials composed of ionic and weakly polarizable atoms where charge carriers are poorly screened from electric fields. We support this argument by studying the electrical properties of $NaPb_mSbSe_{m+2}$ as a function of $NaSbSe_2$ fraction. As shown in Figure 1b and 1c, we observe stronger GB scattering and estimate higher GB energy barriers as increasing amount of

the ionic $NaSbSe_2$ is alloyed into PbSe. We furthermore demonstrate that the GB scattering is strongest in the sulfides ($NaPb_mSbS_{m+2}$) but is completely absent in the tellurides ($NaPb_mSbTe_{m+2}$). Lastly, we discuss how this framework elegantly explains the presence of GB limited electrical conductivity in numerous ionic thermoelectric materials. We suggest how the insight provided by this work gives valuable intuition on engineering the proper microstructure for many emerging thermoelectric materials.

Results and Discussion:

Experimental evidence for grain boundary charge carrier scattering in $NaPb_mSbSe_{m+2}$: Our previous work established that $NaPb_mSbSe_{m+2}$ has atypical electrical transport properties consisting of semiconducting electrical conductivity below 500 K despite being degenerately doped to charge carrier densities over 10^{20} cm^{-3}.[13] At the time, we suggested this behavior to be from GB charge carrier scattering, but without providing direct evidence. Indeed, other models such as ionized impurity scattering can in principle give a similar temperature dependence and have been invoked to explain comparable transport properties in Mg_3Sb_2.[15, 29] Considering this, we sought to obtain conclusive experimental evidence regarding the source of the unusual charge transport properties measured in $NaPb_mSbSe_{m+2}$. To test if the thermally activated scattering is rooted at the GBs, we prepared large grained samples of $NaPb_mSbSe_{m+2}$ with fewer GBs and compared the electrical properties with the data from our previously reported small grained SPS processed materials.[13]

To prepare samples with a reduced number of GBs, we heated vacuum sealed tubes containing the starting reagents to 1473 K and held them at temperature for 5 h. The samples were next slowly cooled from 1473 K to 823 K over 48 h and then brought to room temperature in 12

h. This slow cooling procedure gave time for large grains (mm scale) to nucleate and yielded dense ingots with a relatively low number of GBs. More information on the grain size will be provided by the microscopy date discussed below. Because subsequent pulverization and SPS sintering gives samples with small grains and many boundaries, the as-cast ingots were directly cut and polished into ~3x3x10 mm^3 bars to characterize the electrical properties. The synthesis is presented in greater detail in the experimental section. Powder X-ray diffraction patterns for both the as-cast ingots and SPS processed samples are presented in the supporting information in Figure S1. The diffraction patterns show negligible differences between samples, confirming the expected rocksalt crystal structure with no detectable secondary phases in any of the samples we analyzed.

The primary results are outlined in Figure 2, which shows a comparison of the grain structures and electrical properties of two differently doped samples of $Na_{1+x}Pb_{10-x}SbSe_{12}$ (nominally ~9% $NaSbSe_2$ in PbSe, with additional Na dopant fractions of x = 0.03, 0.15) prepared by slowly cooling the ingots and through rapid quenching and subsequent SPS processing. These compositions were chosen to compare the electrical properties of both lightly and heavily doped samples in small- and large-grained forms. We used electron backscatter diffraction (EBSD) to analyze the grain morphologies of the different samples. Figures 2a and 2b show characteristic EBSD images, demonstrating that while the SPS processed material contains relatively small grains on the order of ~ 50 μm or less in size, the slow cooled ingot has much larger grains on the millimeter scale. This implies a dramatically lower density of GBs in the slow cooled ingot. As anticipated from the GB scattering model, the lower GB density has direct consequences on the electrical conductivity. Most importantly, for both sample pairs (x = 0.03 and 0.15), Figure 2c shows that the semiconducting charge transport observed in the SPS processed samples vanishes in the slow cooled ingots, and the expected metallic behavior is recovered. Furthermore, Figure 2d

demonstrates that the Seebeck coefficients of each pair are nearly identical over the full temperature window, indicating the charge carrier densities are approximately equal between ingot and SPS processed samples. Moreover, because the Seebeck coefficients and PXRD data indicate that each pair of compounds has nominally identical doping and chemical composition, impurity scattering in each should be comparable. As such, the results presented in Figure 2 unambiguously links the thermally activated charge transport to the GBs, providing strong evidence in favor of the GB carrier scattering model.

To further strengthen the case for GB scattering, we also prepared samples with different densities of GBs by passing sample powders through sieves with different mesh sizes prior to SPS sintering. Again, more details on this procedure are given in the experiment section, and PXRD patterns obtained for each sample are shown in Figure S2. Like the slow cooled ingots, the powder patterns confirm the rocksalt structure with negligible secondary phases for each sample. In principle, samples passed through smaller mesh sieves should have on average smaller grains and therefore a greater density of boundaries. Here, we utilized meshes of 53, 70, and 150 μm, as well as one sample that was not sieved. The thermoelectric data for the resulting samples is shown in Figure S7 and again demonstrates a direct link between GBs and low temperature carrier scattering. As the mesh (and presumably the grain) size is decreased, the electrical conductivity is increasingly suppressed under ~500 K, while the values all approximately converge above this temperature. The Seebeck coefficients of these samples are likewise extremely similar, indicating comparable carrier concentrations. Together, the electrical data of the slow-cooled ingots and samples prepared with varying GB density provide substantial experimental support that the low temperature carrier scattering found in $NaPb_mSbSe_{m+2}$ originates from the GBs.

Microscopic characterization of the grain boundaries in $NaPb_mSbQ_{m+2}$: Having directly linked the low temperature charge carrier scattering in $NaPb_mSbSe_{m+2}$ to the GBs, we found it surprising that the chemically similar telluride analogues ($NaPb_mSbTe_{m+2}$) do not show GB charge carrier scattering, and instead exhibit the typical degenerate semiconducting electrical behavior.[31, 32] Moreover, because lead chalcogenide thermoelectrics do not typically feature GB scattering, the apparent uniqueness of the $NaPb_mSbSe_{m+2}$ family warrants an explanation. Our initial hypothesis was that the GBs in $NaPb_mSbSe_{m+2}$ act as sinks for phase or dopant separation, thereby leading to thin resistive barriers along the boundaries that impede the flow of charge carriers. Indeed, small quantities of SnO_2 are known to form along the GBs and dramatically restrict charge transport in polycrystalline SnSe.[24, 34] To investigate if similar phase segregation is occurring in our materials, we performed scanning transmission electron microscopy (STEM) and transmission electron microscopy (TEM) on several samples of SPS-processed $NaPb_mSbSe_{m+2}$ and $NaPb_mSbTe_{m+2}$ to elucidate any structural and chemical differences along the grain boundaries.

Several representative high angle annular dark field-scanning transmission electron microscopy (HAADF-STEM) and high resolution TEM (HRTEM) images of a sample with nominal composition $Na_{1.15}Pb_{9.85}SbSe_{12}$ are presented in Figure 3. Both the HRTEM and STEM images shown in Figures 3a and 3b reveal a clean boundary free of obvious signs of phase segregation. In addition, we conducted energy dispersive X-ray spectroscopy (EDS) elemental maps over the GB regions and display the results in the supporting information in Figure S5. The EDS maps lack evidence for any significant phase or impurity segregation along the boundary, supporting the interpretation of Figures 3a and 3b. Taken together, the microscopy data suggests the GBs in $NaPb_mSbSe_{m+2}$ to be reasonably free of any secondary phase segregation within the

limits of our analysis. Additional STEM-EDS maps of the GBs are provided in Figure S8 in the supporting information and further support the above conclusion.

Since the $NaPb_mSbTe_{m+2}$ compounds do not exhibit GB limited electrical conductivity,[13, 32] we also characterized these materials to compare the GBs with those of the selenides. Samples were prepared following the synthetic protocol outlined in our prior work,[31] and TEM and STEM images of a GB in a telluride sample with nominal composition $Na_{1.10}Pb_{9.90}Sb_{0.85}Te_{12}$ are presented in Figure 3c and 3d. Again, both the high and low magnification STEM images and EDS maps indicate clean GBs without observable phase segregation. EDS maps over the GB region shown in Figure S6 in the supporting information support this interpretation. Therefore, our electron microscopy analysis indicates there is negligible secondary phase segregation at the GBs in either $NaPb_mSbSe_{m+2}$ or $NaPb_mSbTe_{m+2}$. Other techniques, such as atom probe tomography (APT), indicate that some Na often segregates to the GBs in heavily sodium-doped lead chalcogenides,[4, 35-38] yet this does not typically lead to thermally activated conduction in these materials. A different explanation is needed to account for the presence of strong GB scattering in $NaPb_mSbSe_{m+2}$.

Charge carrier trapping at the grain boundaries: Many polycrystalline semiconductors are known to intrinsically host energy barriers localized at the grain boundaries that manifest in thermally activated charge carrier mobility.[25-27] Such a situation is well summarized by Seto, who argues the energy barriers form because the atoms at the GB are more likely to have incomplete atomic bonding, or in other words that the GB region is rich with under coordinated atoms and dangling bonds compared to the bulk. The GB defects can act as trap states that immobilize charge carriers.[22] After trapping electrons or holes, the GBs become electrically charged, creating

potential barriers physically analogous to a double Schottky barrier centered on the boundary. The barriers then strongly impede the flow of charge carriers through the material. Analysis of such a theoretical situation shows that in one dimension, the barrier height at the GBs takes the following form:[22]

$$E_b = \frac{e^2 Q_t^2}{8N\varepsilon} \quad (1)$$

where e is the electron charge, Q_t is the density of trapping states at the GB, N is the concentration of dopant atoms, and ε is the static dielectric permittivity. This equation is derived under the assumption that the doping density is greater than the concentration of GB trap states, which seems reasonable considering that the bulk electrical conductivities and Seebeck coefficients indicate degenerate carrier concentrations. While Equation 1 was derived for a single dimension, we propose that it provides the necessary intuition to understand the GB scattering in our materials. Within the grains, the charge transport is dominated by phonon (deformation potential) scattering as normal; however, the carriers are impeded by the energy barriers at the GBs, and here the conduction is modeled as thermionic emission over the boundary to give electrical conductivity as follows:[22]

$$\sigma_{GB} = e^2 Ln\left(\frac{1}{2\pi m^* k_B T}\right)^{1/2} \exp\left(\frac{-E_b}{k_B T}\right) \quad (2)$$

where L is the grain size, n is the charge carrier density, m^* is the carrier effective mass and k_B is the Boltzmann constant. Using the model developed by Kuo *et al.*, the overall electrical conductivity is calculated by treating the material as a two-phase system consisting of the bulk grain phase and the GB phase. The total electrical conductivity is then modeled by considering the two phases as forming a series circuit to yield[21]:

$$\sigma^{-1} = (1-t)\sigma_G^{-1} + t\sigma_{GB}^{-1} \quad (3)$$

where *t* is a constant representing the fraction of the GB phase. Our analysis using Eqs. 1–3 reveals several important results relevant to $NaPb_mSbQ_{m+2}$ materials that are detailed in the following sections. Additional information regarding use of these equations to analyze the GB scattering in our $NaPb_mSbQ_{m+2}$ materials is given in the supporting information.

Relationship between polarizability and GB charge carrier scattering: If two samples have comparably sized grains, equations 1 and 2 show that the height of the GB potential barriers, and therefore the degree of GB resistance, is linearly proportional to the density of GB trapping states and inversely proportional to the doping level and the dielectric constant. Considering that lead chalcogenides have been extensively studied across a wide range of carrier concentration and with numerous dopants, yet do not typically exhibit strong GB scattering, we propose $NaPb_mSbSe_{m+2}$ is more susceptible to GB scattering because of its relatively low dielectric constant compared to that of pure PbSe. This is intuitive, as smaller values of ε indicate weaker screening of the charge carriers from any electric fields. Moreover, the lower dielectric constant of $NaPb_mSbSe_{m+2}$ can be rationalized with simple chemical principles. Namely, the dielectric constant (and strength of charge carrier screening) is expected to be smaller (weaker) in more ionic and less polarizable crystals than in highly covalent and polarizable compounds. With this in mind, alloying the significantly more ionic $NaSbSe_2$ into PbSe is expected to yield a less polarizable crystal with weaker carrier screening and lower ε than pure PbSe. Furthermore, the argument also explains the lack of GB scattering in the otherwise similar $NaPb_mSbTe_{m+2}$ materials. Because PbTe has a much larger dielectric constant than PbSe, respectively 414 vs. 210 at 300 K,[39, 40] it is reasonable to expect the charge carrier screening in $NaPb_mSbTe_{m+2}$ to be considerably stronger than in $NaPb_mSbSe_{m+2}$, leading to weaker GB scattering in the tellurides as we indeed observe.

To support the qualitative picture outlined above, we used density functional theory to calculate the relative static dielectric constants of each lead chalcogenide and $NaSbQ_2$ compound, and the results are presented in Table 1. While the calculated values for the pure lead chalcogenides are somewhat higher than the experimental numbers,[39-41] our results are in general agreement with other DFT calculated dielectric constants for these materials. Crucially, the calculated dielectric constants trend as anticipated, with three to five times higher values for the pure lead chalcogenides, which are all greater than 328, compared to their respective $NaSbQ_2$ analogues which are all under 113. Moreover, the calculated values of ε decrease moving down the periodic table from PbTe (501) to PbS (328), as anticipated by the polarizability of each compound. Somewhat surprisingly, $NaSbTe_2$ has the smallest calculated dielectric constant of the $NaSbQ_2$ materials; however, because the values of ε are all much larger for the pure lead chalcogenides, we do not anticipate this to finding to alter our analysis.

In light of the above calculations and discussion, we sought to provide direct experimental evidence linking the GB scattering to the charge carrier screening in $NaPb_mSbSe_{m+2}$. We prepared and investigated the electrical transport properties of p-type doped $NaPb_{20}SbSe_{22}$ (m = 20, ~4% $NaSbSe_2$) and $NaPb_6SbSe_8$ (m = 6, ~14% $NaSbSe_2$) and compared the data with our previously reported $NaPb_{10}SbSe_{12}$ (m = 10, ~9% $NaSbSe_2$) materials.[13] We anticipated that the charge carriers in more PbSe-rich (higher m) compositions would be more strongly screened than in $NaSbSe_2$-rich (lower m) phases, and therefore have the weakest GB scattering. In order to make a meaningful comparison between samples, it is imperative for the materials to have similarly sized grains. Because the synthesis, grinding, sieving, sintering procedures for each compound were identical (see experimental section), we believe the assumption of comparable grain sizes is reasonable. The measured electrical data for all m = 20 and m = 6 samples of $NaPb_mSbSe_{m+2}$ is

shown in the supporting information in Figure S8. Inspection of the data clearly shows that the temperature dependence of the electrical conductivities of every m = 20 sample is much closer to the expected metallic behavior than that of the m = 6 samples, which feature strongly suppressed and thermally activated electrical conductivity below ~ 550 K. These factors provide qualitative evidence in support of the carrier screening hypothesis.

To provide a more quantitative argument, we used Equations 2 and 3 to estimate the height of the GB energy barriers in our samples. If the resistance from the GBs is sufficiently strong such that $\sigma_G >> \sigma_{GB}$, then the bulk contribution to the electrical conductivity is masked by the GBs and Equation 3 can be approximated as $\sigma \approx \sigma_{GB}$. Therefore, over the temperature range dominated by GB scattering, Equation 2 approximates the electrical conductivity and gives thermally activated conduction. Importantly, Equation 2 indicates that plotting $\ln\sigma$ vs. $1/k_BT$ should yield a straight line with a slope of $-E_b$ if the carrier concentration remains constant with temperature.[22] Here, we selected representative samples from one of each of our m = 6, 10, 20 sets of compounds and display their electrical conductivities in Figure 4a. Because Equation 1 shows that the energy barriers will also be sensitive to the doping density, these samples were chosen to have similar values of n_H to provide as close a comparison as possible. The variable-temperature Hall effect data is found in Figure 4b and confirms that the samples have comparable hole densities of ~1–1.5x10^{20} cm^{-3} that remain relatively constant with heating below ~600 K.

Figure 4c shows the plots of $\ln\sigma$ vs. $1/k_BT$, and as anticipated, each gives a reasonably linear slope over the low temperature GB dominated regime. The activation barriers extracted from the slopes increase with $NaSbSe_2$ fraction, from 1.6 meV for m = 20 to 68 meV for the m = 6 sample. To best eliminate any contribution from the small temperature dependence of the charge carrier densities, we moreover used the charge carrier mobilities μ_H estimated from Figures 4a and 4c to

plot $\ln\mu_H$ vs. $1/k_BT$ for the same samples. The data is given in the supporting information in Figure S9, and we estimate similar barrier heights of 7.6, 44, and 69 meV for m = 20, 10, and 6 respectively. The above analysis therefore provides direct evidence that at comparable charge carrier concentrations, and for samples with similar bulk conductivity, more $NaSbSe_2$-rich members of the $NaPb_mSbSe_{m+2}$ family have larger GB energy barriers than the PbSe-rich phases, as predicted considering the chemical arguments discussed above.

Lastly, we also investigated the electrical properties of PbS–$NaSbS_2$ alloys ($NaPb_mSbS_{m+2}$). Because the dielectric constant of PbS is measured to be ~169 at 300 K,[41] lower than that of PbSe and PbTe, we predicted $NaPb_mSbS_{m+2}$ to have the strongest GB scattering of the $NaPb_mSbQ_{m+2}$ (Q = S, Se, Te) materials for the same value of m. The electrical conductivities of the p-type doped $Na_{1+x}Pb_{20-x}SbS_{22}$ (~4% $NaSbS_2$ in PbS) samples are displayed in Figure 5a and clearly indicate strong GB scattering, with semiconducting behavior up to 600 K and metallic temperature dependence above. Likewise, the Seebeck coefficients shown in Figure 5b increase with heating over the full range of temperatures, typical of degenerate semiconductors. While we did not conduct variable temperature Hall effect measurements on these samples, degenerate charge carrier densities of 5–15x10^{19} cm^{-3} are confirmed by room-temperature measurements and shown in the supporting information in Table S1. Qualitatively, comparing the data discussed here with the transport properties of the m = 20 selenides shown in Figures 4 and S8, the sulfides clearly exhibit both lower electrical conductivity and semiconducting-like behavior that persists over a greater range of temperatures, both suggesting stronger GB scattering. The plots of $\ln\sigma$ vs. $1/k_BT$ for the x = 0.10 and 0.15 samples are presented in Figure 5c and confirm this suspicion, with estimated energy barriers of 62 and 73 meV respectively. We excluded the x = 0.05 sample from this analysis, as it was too lightly doped and showed influence of intrinsic conduction, leading to

an unphysical barrier height of ~ 220 meV. Clearly, the energy barriers estimated for the m = 20 sulfides are significantly greater than those of the m = 20 selenides.

In summary, we observe stronger GB scattering in the more ionic $NaPb_mSbS_{m+2}$ family than in $NaPb_mSbSe_{m+2}$, which in turn displays stronger scattering than the most polarizable $NaPb_mSbTe_{m+2}$ materials. Likewise, $NaSbSe_2$–rich phases in the $NaPb_mSbSe_{m+2}$ family generally have stronger GB scattering than the PbSe–rich compositions. The energy barriers extracted from the temperature-dependent electrical conductivities support these conclusions. Overall, the above analysis of the GB scattering in the $NaPb_mSbQ_{m+2}$ families provides strong evidence that their respective susceptibilities to GB limited electrical conductivity is driven in large part by their different dielectric permittivities and that this can be rationalized with intuitive chemical principles that consider the polarizability of the atoms in each material.

Broader Scope: relevance of dielectric screening to GB scattering in emerging thermoelectric materials: The analysis and insight presented above can be expanded to other reported thermoelectric materials that have GB limited charge transport. As discussed above, one expects stronger GB scattering in more ionic and less polarizable crystals. Indeed, an examination of the literature supports this intuition, as GB limited behavior is regularly reported in Zintl antimonide compounds such as Mg_3Sb_2,[15, 21] $KAlSb_4$,[16] (Hf,Zr)CoSb,[17] Sr_3GaSb_3,[42] NbFeSb,[18] $Ca_5Al_2Sb_6$,[43] and Ca_3AlSb,[44] as well as other emerging thermoelectric materials like Mg_2Si.[45] Considering that these compounds are all composed of relatively small and less polarizable ions than the classic thermoelectric lead and bismuth chalcogenides, the observed GB scattering is not surprising in light of the above discussion. Indeed, we also calculated dielectric constants for Mg_3Sb_2, NbFeSb, TiCoSb, and Mg_2Si and show the results in Table 1. Our calculated values of ε for these

compounds are among the smallest of all materials considered in this study, suggesting these compounds to be highly prone to GB carrier scattering. Our work therefore provides a rational explanation of the GB scattering in a host of different heavily doped thermoelectric materials and gives an intuitive chemical guideline for anticipating what materials will be most prone to GB limited electronic conduction.

A generally accepted paradigm in thermoelectric research is that small grains are advantageous to maximize phonon scattering, and indeed, an enormous amount of work has focused on both preparing materials with minimal grain size and engineering the grain boundaries to be rich with defects and dislocations in order to maximize GB phonon scattering and achieve extremely low lattice thermal conductivity.[4, 6, 46, 47] In this context, our work provides important insight into the proper engineering of high-performance thermoelectric materials. While such strategies are proven to be effective in highly polarizable materials like lead and bismuth chalcogenides, the results discussed here indicate that small grains are undesirable in more ionic thermoelectric materials such as $NaPb_mSbQ_{m+2}$ (Q = Se, S) and Zintl antimonides. In these cases, it may be more advantageous to prepare samples with large grains to mitigate the charge carrier scattering at the GBs and ensure high electrical mobility.

To support this proposal, we note that large grained Mg_3Sb_2 is reported to have superior thermoelectric performance to small grained samples owing to the improved charge carrier mobility and power factor at lower temperatures.[21, 48, 49] Furthermore, the figures of merit of single crystalline SnSe are markedly superior to polycrystalline forms, and recent work to overcome the severe GB resistance and poor electrical conductivity in polycrystalline SnSe achieved performance comparable to the single crystals.[34] We moreover show the figures of merit for large- and small-grained forms of $NaPb_mSbSe_{m+2}$ in Figures S12 and S13 of the supporting information.

The *ZT*s are significantly enhanced in large grained forms of the more lightly doped samples, and more modestly improved at low temperature in the heavily doped samples. Therefore, we see varying degrees of enhancement in all large grained samples. In general, we anticipate the degree of enhancement to the *ZT* will vary from material to material. In compounds with intrinsically short phonon mean free path, larger grains would be more strongly favored, as the GBs would already have negligible contribution to the lattice thermal conductivity. However, in compounds where the intrinsic phonon mean free path is sufficiently long, the gains achieved by increasing the grain size to improve the electrical mobility may be more modest. Furthermore, because the charge carriers are less screened in lightly doped compounds,[22] enhancement from eliminating GB scattering may be more significant, as we observe here. While the paradigm of minimizing the grain size is deeply entrenched in the thermoelectric literature, this work shows that GB scattering is an often overlooked impediment to engineering high performance thermoelectrics, and researchers working with more ionic and less polarizable semiconductors should be wary of the potential need to suppress its effects.

Summary and conclusions:

We investigated the electrical transport properties of degenerately doped polycrystalline $NaPb_mSbQ_{m+2}$ (Q = S, Se, Te) thermoelectric materials. Despite being degenerately doped, both the selenide and sulfide materials show irregular semiconducting electrical conductivities under 400-600 K, while the tellurides behave normally. We directly show the thermally activated transport comes from carrier scattering at the GBs and demonstrate that the expected metallic conduction can be recovered by preparing large grained samples with a reduced density of grain boundaries. Because our microscopy investigations did not find any unusual phase or dopant

segregation at the GBs in the $NaPb_mSbQ_{m+2}$ materials, we attribute the differing transport properties to the relative dielectric permittivity of each respective $NaPb_mSbQ_{m+2}$ family. In particular, the tellurides feature relatively strong charge carrier screening and negligible GB scattering, while the much less polarizable sulfides exhibit the greatest degree of GB scattering. We moreover show that DFT calculated dielectric constants and experimental estimates of the GB energy barriers support this picture. We finally suggest that weak dielectric screening explains why other emerging thermoelectrics, such as Zintl antimonides, are also reported to have strong GB scattering. This work therefore provides a useful and intuitive chemical guideline for anticipating what materials will be prone to GB scattering. Based on this analysis, we anticipate that the traditional paradigm of minimizing grain size to be inadvisable for these materials and suggest that rationally preparing larger (meso-scale) grained samples may be beneficial to eliminate the GB scattering and improve the low temperature power factors.

Experimental details:

Synthesis and processing: The starting materials were Pb wire (99.99%, American Elements, USA), Se shot (99.99%, American Elements, USA), S pieces (99.99%, American Elements), Sb shot (99.999%, American Elements, USA), and Na cubes (99.95%, Sigma Aldrich). Before synthesis, a razor blade was used to scrape the surface oxidation off the lead and sodium. All sodium was handled in a N_2 filled glovebox.

SPS processed samples: Polycrystalline ingots were first synthesized by weighing stoichiometric quantities of each element according to the desired nominal compositions into 13 mm diameter carbon coated fused silica tubes that were then flame sealed at ~$2x10^{-3}$ Torr. Typical samples used 15 grams of total starting material for the selenides and 10 grams for the sulfides. The tubes were

heated in a box furnace to 773 K over 12 h, held for 2 h, then heated to 1473 K over 7 h where they dwelled at temperature for 5 h. The tubes were next quenched in ice water followed by annealing at 773 K for 12 h. After annealing, the tubes were again quenched in water, and the ingots were removed and ground to a fine powder with a mortar and pestle. We attempted to ensure homogeneous powder and grain size by passing the powdered samples through a 53 μm mesh sieve. The samples were then each loaded into 12.7 mm graphite dies and sintered into dense pellets by spark plasma sintering (SPS-211LX, Fuji Electronic Industrial Co. Ltd). The sintering process was conducted under dynamic vacuum at 823 K for the selenides and at 873 K for the sulfides. In both cases the samples were held at the desired temperature for 10 min under 40 MPa of uniaxial pressure before being cooled to room temperature. To characterize the electrical properties, the pellets were finally cut and polished into bars and squares of approximate dimensions 3x3x10 mm^3 and 6x6x2 mm^3. The cuts were made such that transport measurements were conducted perpendicular to the pressing direction in the SPS.

To study the effect of GB density on the electrical properties of the $NaPb_mSbSe_{m+2}$ family, we also prepared samples with differing grain sizes. This was accomplished by following the same synthetic procedure outlined above, but after crushing and grinding the ingots, the resulting powders were passes through sieves with different mesh sizes. We utilized mesh sizes of 53, 70, and 150 μm, and one sample was only briefly crushed and left un-sieved to (in principle) give the largest grains. These samples were then sintered and prepared for measurements under the conditions discussed in the preceding paragraph.

Large grained as-cast ingots: To prepare samples with the largest possible grains and lowest number of GBs, elements were first weighed at sealed in 13 mm diameter carbon-coated tubes as discussed above. We used the same heating profile to bring the tubes to 1473 K, and then held the

samples at temperature for 5 hours. Instead of rapidly quenching, the tubes were next slowly cooled to 823 K over 48 h before finally being brought to room temperature in 12 h. The slow cooling process gave enough time for large grains to nucleate. To characterize the thermoelectric properties, the as-cast ingots were carefully removed from the tubes and directly cut/polished into 3x3x10 mm^3 bars like the SPS sintered pellets discussed above.

Electrical conductivity and Seebeck Coefficient: With the 3x3x10 mm^3 bars, the electrical conductivities and Seebeck coefficients were measured between room temperature and 873 K using an Ulvac Riko ZEM-3 instrument. To limit outgassing at elevated temperatures, the bars were spray-coated with boron nitride aerosol prior to measurements except at the locations needed for contacts with the electrodes and thermocouples. The measurements were conducted under partial He backpressure. The uncertainty in the electrical measurements from a ZEM-3 instrument is approximately 5%. We measured the properties upon both heating and cooling. For the samples with strong GB scattering, hysteresis was often observed between first heating and cooling profile; however, the data was consistent with additional thermal cycling (see our previous work and Figure S11 in the supporting information for a more detailed discussion[13]). As such, all data in this manuscript was taken from the cooling profile.

Hall effect: The Hall effect measurements were completed using two different homebuilt systems. One used an AC 4-probe method with excitation fields of ±0.5 Tesla. The system uses an air-bore, helium-cooled superconducting magnet to generate the field within a high temperature oven that surrounds the Ar-filled sample probe. The second setup utilizes Van der Pauw geometry with magnetic fields of ~2T. The carrier densities were calculated from the Hall coefficient assuming a single carrier band, i.e., $n_H = 1/eR_H$, where R_H is the Hall coefficient.

Microscopy characterization: Grain size was illustrated through the use of Electron Backscattered Diffraction (EBSD). EBSD samples were prepared by first cold mounting samples in an epoxy to improve the quality of polishing and to reduced sample cracking and breaking during subsequent preparation steps. Samples were then ground using 600, 800, and 1200 grit SiC paper for 10 min each, while using ethanol as a water free lubricant. Next samples were polished using 1 μm and 0.1 μm glycol-based (water free) diamond slurry for 30 and 45 min respectively. EBSD was performed using an FEI Quanta 650 ESEM at 30 kV.

To investigate the grain boundaries of $NaPb_mSbTe_{m+2}$ and $NaPb_mSbSe_{m+2}$ compounds, we performed a combination of High-Resolution Transmission Electron Microscopy (HREM) and Scanning Transmission Electron Microscopy-Energy Dispersive Spectroscopy (STEM-EDS). Samples were prepared for S/TEM analysis by conventional bulk TEM sample preparation method which includes grinding and polishing, dimpling, and finally argon ion milling. Like the first steps in EBSD sample preparation, the samples were ground on the top side using 600, 800, and 1200 grit SiC paper for 10 min each using a grinding wheel. Samples were then polished for 30 min using 1-μm glycol-based diamond slurry. A TEM grid was then attached to this polished surface using M-bond. The sample was then flipped over and the backside was ground to approximately 50 μm in thickness, again using 600, 800, and 1200 grit SiC paper. The sample was then dimpled and placed in a Fischione 1050 TEM Mill. The samples were milled at 4 kV at an angle of 6° until a hole was formed, then milled at 2 kV at 4° until the hole was widened slightly (denoted by the edge features of the hole changing shape). The sample was then polished at 1 kV and 0.3 kV for 30 minutes each at 4°. HREM and STEM were then performed at 200 kV using a JEOL JEM-2100 FasTem.

Calculations of the dielectric constants: The dielectric constant calculations in this study were performed using density functional perturbation theory (DFPT)[50] as implemented in Vienna ab initio simulation package (VASP).[51] We used Perdew–Burke–Ernzerhof (PBE) formulation of the exchange-correlation energy functional derived under a generalized–gradient approximation (GGA).[52] Plane-wave basis sets were truncated at an energy cutoff of 450 eV, and a gamma-centered k-point mesh with a density of ~16,000 k-points per reciprocal atom (KPPRA) was used. All structures were relaxed with respect to cell vectors and their internal degrees of freedom until forces on all atoms were less than 0.1 eV nm^{-1}.

Acknowledgements:

This work is supported by the U.S Department of Energy, Office of Science and Office of Basic Energy Sciences under award number DE-SC0014520. This work made use of the EPIC facility of Northwestern University's NU*ANCE* Center, which has received support from the Soft and Hybrid Nanotechnology Experimental (SHyNE) Resource (NSF ECCS-1542205); the MRSEC program (NSF DMR-1720139) at the Materials Research Center; the International Institute for Nanotechnology (IIN); the Keck Foundation; and the State of Illinois, through the IIN. This work also made use of the MatCI Facility which receives support from the MRSEC Program (NSF DMR- 1720139) of the Materials Research Center at Northwestern University. This material is based upon work supported by the National Science Foundation Graduate Research Fellowship under Grant No. DGE-1324585. GJS, SA, MW, JJH acknowledge the support of award 70NANB19H005 from U.S. Department of Commerce, National Institute of Standards and Technology as part of the Center for Hierarchical Materials Design (CHiMaD)

References:

1. D. Champier, *Energy Convers. Manage.*, 2017, **140**, 167-181.
2. Y. Zhang, *ACS Energy Letters*, 2018, **3**, 1523-1524.
3. Y. Pei, X. Shi, A. LaLonde, H. Wang, L. Chen and G. J. Snyder, *Nature*, 2011, **473**, 66-69.
4. K. Biswas, J. He, I. D. Blum, C.-I. Wu, T. P. Hogan, D. N. Seidman, V. P. Dravid and M. G. Kanatzidis, *Nature*, 2012, **489**, 414-418.
5. G. Tan, F. Shi, S. Hao, L.-D. Zhao, H. Chi, X. Zhang, C. Uher, C. Wolverton, V. P. Dravid and M. G. Kanatzidis, *Nature Communications*, 2016, **7**, 12167.

6. Y. Xiao, J.-y. Yang, Q.-h. Jiang, L.-w. Fu, Y.-b. Luo, M. Liu, D. Zhang, M.-y. Zhang, W.-x. Li, J.-y. Peng and F.-q. Chen, *Journal of Materials Chemistry A*, 2014, **2**, 20288-20294.
7. H. Liu, X. Shi, F. Xu, L. Zhang, W. Zhang, L. Chen, Q. Li, C. Uher, T. Day and G. J. Snyder, *Nature Materials*, 2012, **11**, 422.
8. L.-D. Zhao, S.-H. Lo, Y. Zhang, H. Sun, G. Tan, C. Uher, C. Wolverton, V. P. Dravid and M. G. Kanatzidis, *Nature*, 2014, **508**, 373-377.
9. L. D. Zhao, D. Berardan, Y. L. Pei, C. Byl, L. Pinsard-Gaudart and N. Dragoe, 2010, **97**, 092118.
10. D. Kraemer, J. Sui, K. McEnaney, H. Zhao, Q. Jie, Z. F. Ren and G. Chen, *Energy & Environmental Science*, 2015, **8**, 1299-1308.
11. J. Zhang, L. Song, S. H. Pedersen, H. Yin, L. T. Hung and B. B. Iversen, *Nature Communications*, 2017, **8**, 13901.
12. Y. Tang, Z. M. Gibbs, L. A. Agapito, G. Li, H.-S. Kim, Marco B. Nardelli, S. Curtarolo and G. J. Snyder, *Nature Materials*, 2015, **14**, 1223-1228.
13. T. J. Slade, T. P. Bailey, J. A. Grovogui, X. Hua, X. Zhang, J. J. Kuo, I. Hadar, G. J. Snyder, C. Wolverton, V. P. Dravid, C. Uher and M. G. Kanatzidis, *Advanced Energy Materials*, 2019, **9**, 1901377.
14. T.-R. Wei, G. Tan, X. Zhang, C.-F. Wu, J.-F. Li, V. P. Dravid, G. J. Snyder and M. G. Kanatzidis, *J. Am. Chem. Soc.*, 2016, **138**, 8875-8882.
15. J. Mao, J. Shuai, S. Song, Y. Wu, R. Dally, J. Zhou, Z. Liu, J. Sun, Q. Zhang, C. dela Cruz, S. Wilson, Y. Pei, D. J. Singh, G. Chen, C.-W. Chu and Z. Ren, *Proceedings of the National Academy of Sciences*, 2017, **114**, 10548-10553.
16. B. R. Ortiz, P. Gorai, L. Krishna, R. Mow, A. Lopez, R. McKinney, V. Stevanović and E. S. Toberer, *Journal of Materials Chemistry A*, 2017, **5**, 4036-4046.
17. Q. Qiu, Y. Liu, K. Xia, T. Fang, J. Yu, X. Zhao and T. Zhu, *Advanced Energy Materials*, 2019, **9**, 1803447.
18. R. He, D. Kraemer, J. Mao, L. Zeng, Q. Jie, Y. Lan, C. Li, J. Shuai, H. S. Kim, Y. Liu, D. Broido, C.-W. Chu, G. Chen and Z. Ren, *Proceedings of the National Academy of Sciences*, 2016, **113**, 13576-13581.
19. Z.-Z. Luo, S. Hao, X. Zhang, X. Hua, S. Cai, G. Tan, T. P. Bailey, R. Ma, C. Uher, C. Wolverton, V. P. Dravid, Q. Yan and M. G. Kanatzidis, *Energy & Environmental Science*, 2018, **11**, 3220-3230.
20. I. U. I. Ravich, B. A. Efimova and I. A. Smirnov, *Semiconducting lead chalcogenides*, Plenum Press, New York, 1970.
21. J. J. Kuo, S. D. Kang, K. Imasato, H. Tamaki, S. Ohno, T. Kanno and G. J. Snyder, *Energy & Environmental Science*, 2018, DOI: 10.1039/C7EE03326E.
22. J. Y. W. Seto, *J. Appl. Phys.*, 1975, **46**, 5247-5254.
23. J. W. Orton and M. J. Powell, *Rep. Prog. Phys.*, 1980, **43**, 1263-1307.
24. S. Wang, S. Hui, K. Peng, T. P. Bailey, X. Zhou, X. Tang and C. Uher, *Journal of Materials Chemistry C*, 2017, **5**, 10191-10200.
25. K. Lipskis, A. Sakalas and J. Viščakas, *physica status solidi (a)*, 1971, **5**, 793-801.
26. J. W. Orton, *Thin Solid Films*, 1981, **86**, 351-357.
27. C. R. M. Grovenor, *Journal of Physics C: Solid State Physics*, 1985, **18**, 4079.
28. J. Levinson, F. R. Shepherd, P. J. Scanlon, W. D. Westwood, G. Este and M. Rider, *J. Appl. Phys.*, 1982, **53**, 1193-1202.

29. L. Pan, S. Mitra, L.-D. Zhao, Y. Shen, Y. Wang, C. Felser and D. Berardan, *Adv. Funct. Mater.*, 2016, **26**, 5149-5157.
30. K. F. Cai, X. R. He, M. Avdeev, D. H. Yu, J. L. Cui and H. Li, *J. Solid State Chem.*, 2008, **181**, 1434-1438.
31. T. J. Slade, J. A. Grovogui, S. Hao, T. P. Bailey, R. Ma, X. Hua, A. Guéguen, C. Uher, C. Wolverton, V. P. Dravid and M. G. Kanatzidis, *J. Am. Chem. Soc.*, 2018, **140**, 7021-7031.
32. P. F. P. Poudeu, J. D'Angelo, A. D. Downey, J. L. Short, T. P. Hogan and M. G. Kanatzidis, *Angew. Chem. Int. Ed.*, 2006, **45**, 3835-3839.
33. M. Zhou, J.-F. Li and T. Kita, *J. Am. Chem. Soc.*, 2008, **130**, 4527-4532.
34. Y. K. Lee, Z. Luo, S. P. Cho, M. G. Kanatzidis and I. Chung, *Joule*, 2019, **3**, 719-731.
35. K. Biswas, J. He, Q. Zhang, G. Wang, C. Uher, V. P. Dravid and M. G. Kanatzidis, *Nat Chem*, 2011, **3**, 160-166.
36. J. He, I. D. Blum, H.-Q. Wang, S. N. Girard, J. Doak, L.-D. Zhao, J.-C. Zheng, G. Casillas, C. Wolverton, M. Jose-Yacaman, D. N. Seidman, M. G. Kanatzidis and V. P. Dravid, *Nano Lett.*, 2012, **12**, 5979-5984.
37. I. D. Blum, D. Isheim, D. N. Seidman, J. He, J. Androulakis, K. Biswas, V. P. Dravid and M. G. Kanatzidis, *J. Electron. Mater.*, 2012, **41**, 1583-1588.
38. Y.-J. Kim, L.-D. Zhao, M. G. Kanatzidis and D. N. Seidman, *ACS Applied Materials & Interfaces*, 2017, **9**, 21791-21797.
39. in *Non-Tetrahedrally Bonded Elements and Binary Compounds I*, eds. O. Madelung, U. Rössler and M. Schulz, Springer Berlin Heidelberg, Berlin, Heidelberg, 1998, DOI: 10.1007/10681727_719, pp. 1-10.
40. in *Non-Tetrahedrally Bonded Elements and Binary Compounds I*, eds. O. Madelung, U. Rössler and M. Schulz, Springer Berlin Heidelberg, Berlin, Heidelberg, 1998, DOI: 10.1007/10681727_895, pp. 1-10.
41. in *Non-Tetrahedrally Bonded Elements and Binary Compounds I*, eds. O. Madelung, U. Rössler and M. Schulz, Springer Berlin Heidelberg, Berlin, Heidelberg, 1998, DOI: 10.1007/10681727_881, pp. 1-6.
42. A. Zevalkink, W. G. Zeier, G. Pomrehn, E. Schechtel, W. Tremel and G. J. Snyder, *Energy & Environmental Science*, 2012, **5**, 9121-9128.
43. E. S. Toberer, A. Zevalkink, N. Crisosto and G. J. Snyder, *Adv. Funct. Mater.*, 2010, **20**, 4375-4380.
44. W. G. Zeier, A. Zevalkink, E. Schechtel, W. Tremel and G. J. Snyder, *J. Mater. Chem.*, 2012, **22**, 9826-9830.
45. J. de Boor, T. Dasgupta, H. Kolb, C. Compere, K. Kelm and E. Mueller, *Acta Mater.*, 2014, **77**, 68-75.
46. J. Ko, J.-Y. Kim, S.-M. Choi, Y. S. Lim, W.-S. Seo and K. H. Lee, *Journal of Materials Chemistry A*, 2013, **1**, 12791-12796.
47. K. Nielsch, J. Bachmann, J. Kimling and H. Böttner, *Advanced Energy Materials*, 2011, **1**, 713-731.
48. T. Kanno, H. Tamaki, H. K. Sato, S. D. Kang, S. Ohno, K. Imasato, J. J. Kuo, G. J. Snyder and Y. Miyazaki, *Appl. Phys. Lett.*, 2018, **112**, 033903.
49. M. Wood, J. J. Kuo, K. Imasato and G. J. Snyder, *Adv. Mater.*, 2019, **31**, 1902337.
50. W. Kohn, A. D. Becke and R. G. Parr, *The Journal of Physical Chemistry*, 1996, **100**, 12974-12980.

51. G. Kresse and J. Furthmüller, *Phys. Rev. B: Condens. Matter Mater. Phys.*, 1996, **54**, 11169.
52. J. P. Perdew, K. Burke and M. Ernzerhof, *Phys. Rev. Lett.*, 1996, **77**, 3865.

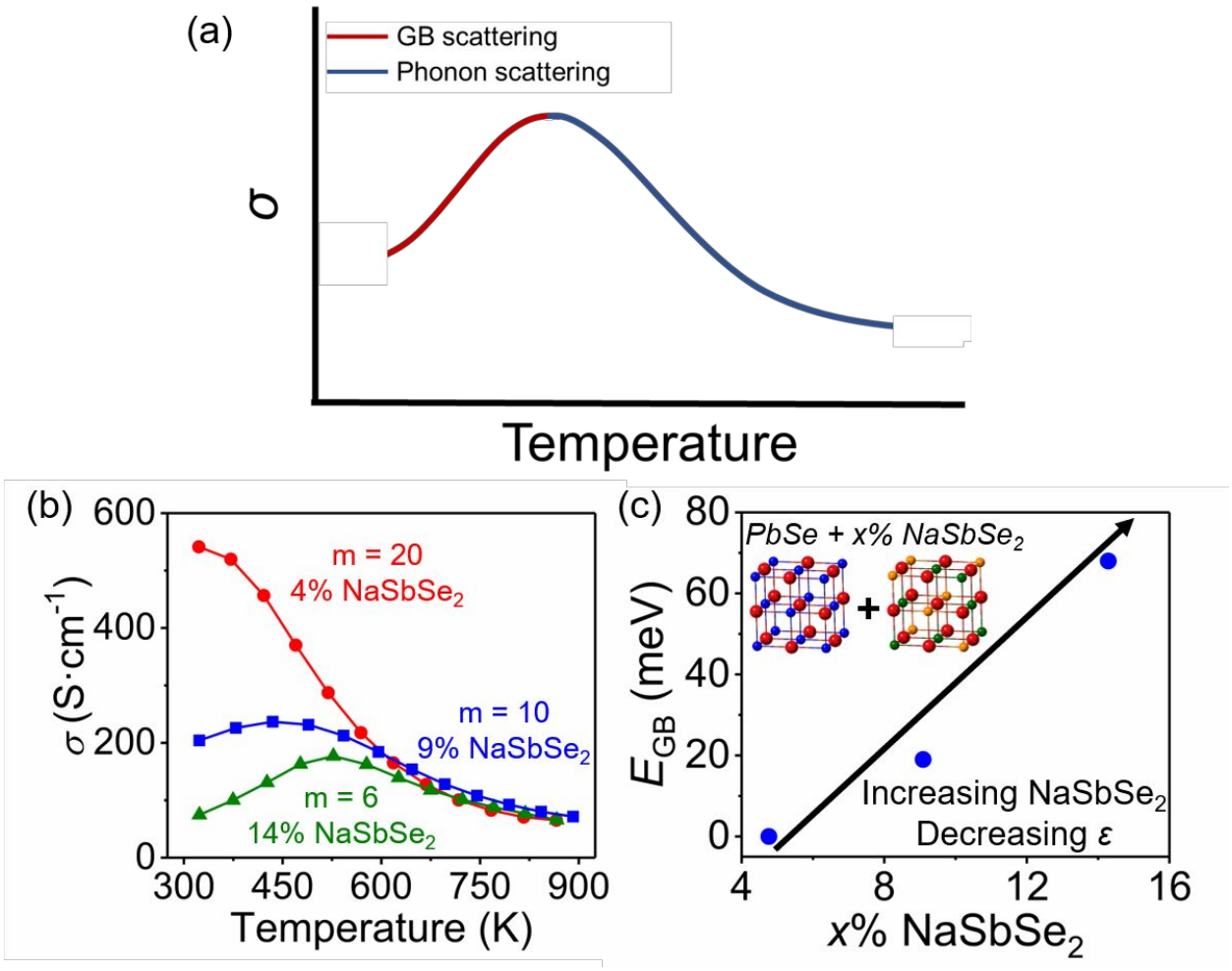

Figure 1: (a) Illustration of the unusual temperature dependence of the electrical conductivity observed in thermoelectric materials such as PbSe-$NaSbSe_2$ ($NaPb_mSbSe_{m+2}$), Mg_3Sb_2, SnSe, and Zintl antimonides. At low temperatures, charge carriers are scattered at the grain boundaries, leading to thermally activated conduction. Above a threshold temperature, the expected phonon scattering dominates the electronic transport. (b) Variable-temperature electrical conductivities for PbSe alloyed with ~4, 9, and 14 percent $NaSbSe_2$. The electrical conductivities are increasingly suppressed under ~600 K for greater $NaSbSe_2$ fraction. (c) Estimated energy barriers at the GBs for the samples in (b). As the more ionic $NaSbSe_2$ is added to PbSe, the charge carrier screening is weakened (decreased ε) and the barrier heights increase. The inset in (c) is a cartoon illustration of alloying $NaSbSe_2$ into PbSe to form $NaPb_mSbSe_{m+2}$.

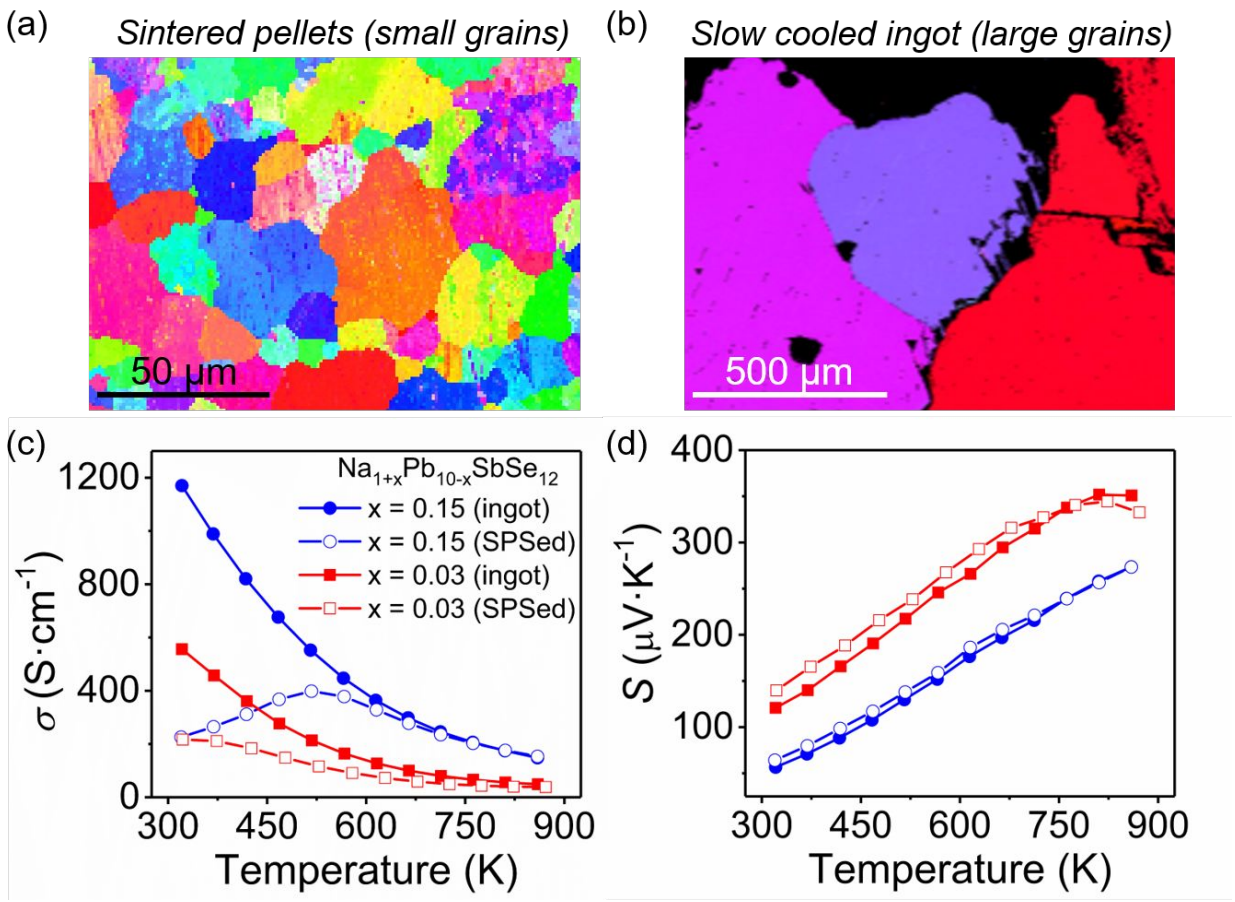

Figure 2: Electron backscatter diffraction (EBSD) images showing the grain structure of $Na_{1.15}Pb_{9.85}SbSe_{12}$ samples prepared by (a) water quenching followed by powdering and SPS sintering and (b) slow cooling of ingots. Each individually colored region represents a single grain. Comparison of the (c) electrical conductivities and (d) Seebeck coefficients for large grained (slow cooled ingots), and small grained (SPS sintered pellets) Na-doped $Na_{1+x}Pb_{10-x}SbSe_{12}$. The closed points represent data for the large grained samples and the open points represent the small grained samples.

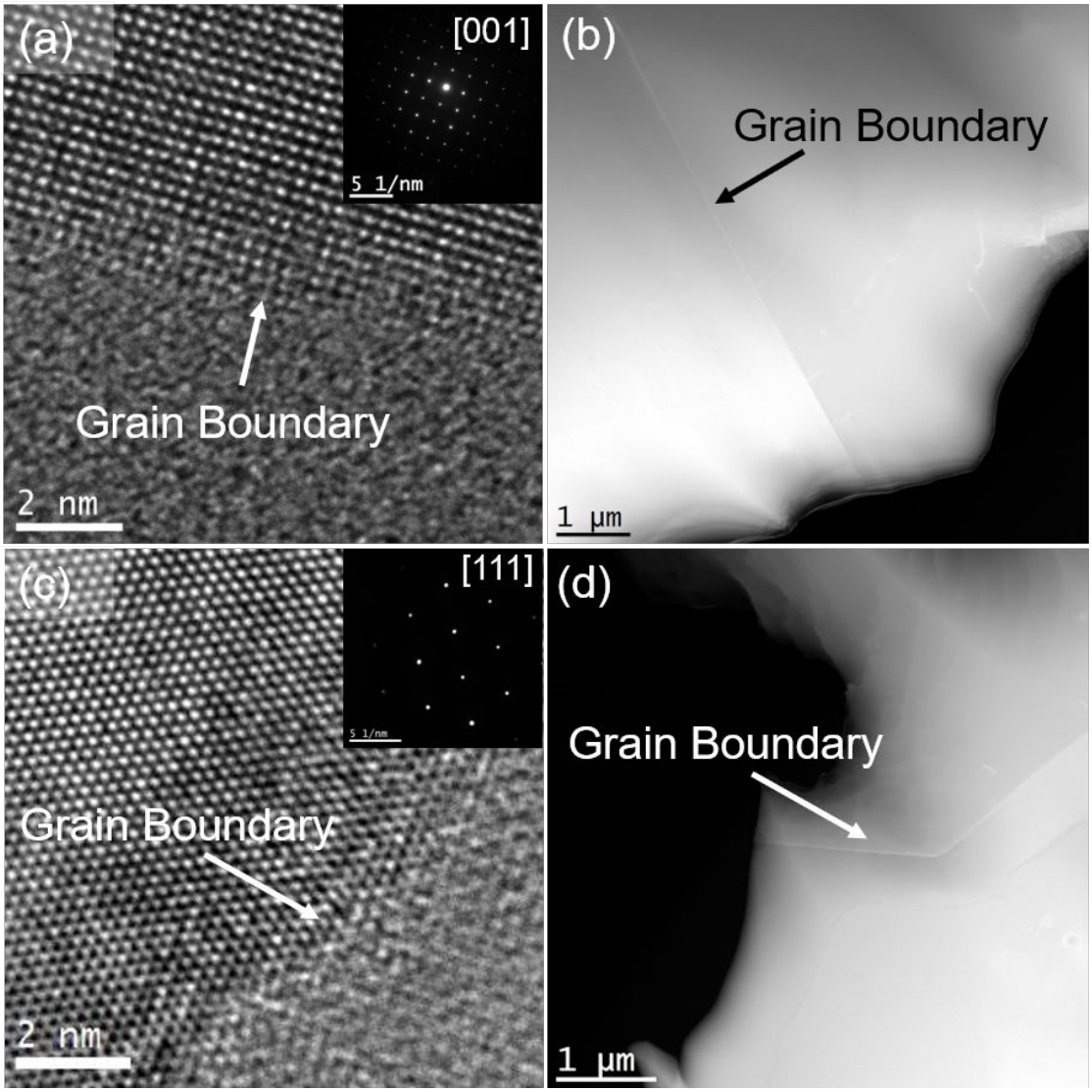

Figure 3: (a) A characteristic high resolution TEM image of a grain boundary in a m = 10 selenide sample with nominal composition $Na_{1.15}Pb_{9.85}SbSe_{12}$. The image shows a clean boundary with no evidence for secondary phase segregation. The inset displays a selected area electron diffraction pattern showing only the expected rocksalt spots. (b) A HAADF-STEM image of another GB in the same sample also showing a clean boundary. (c) and (d) are the same for telluride samples with nominal composition $Na_{1.10}Pb_{9.90}Sb_{0.85}Te_{12}$.

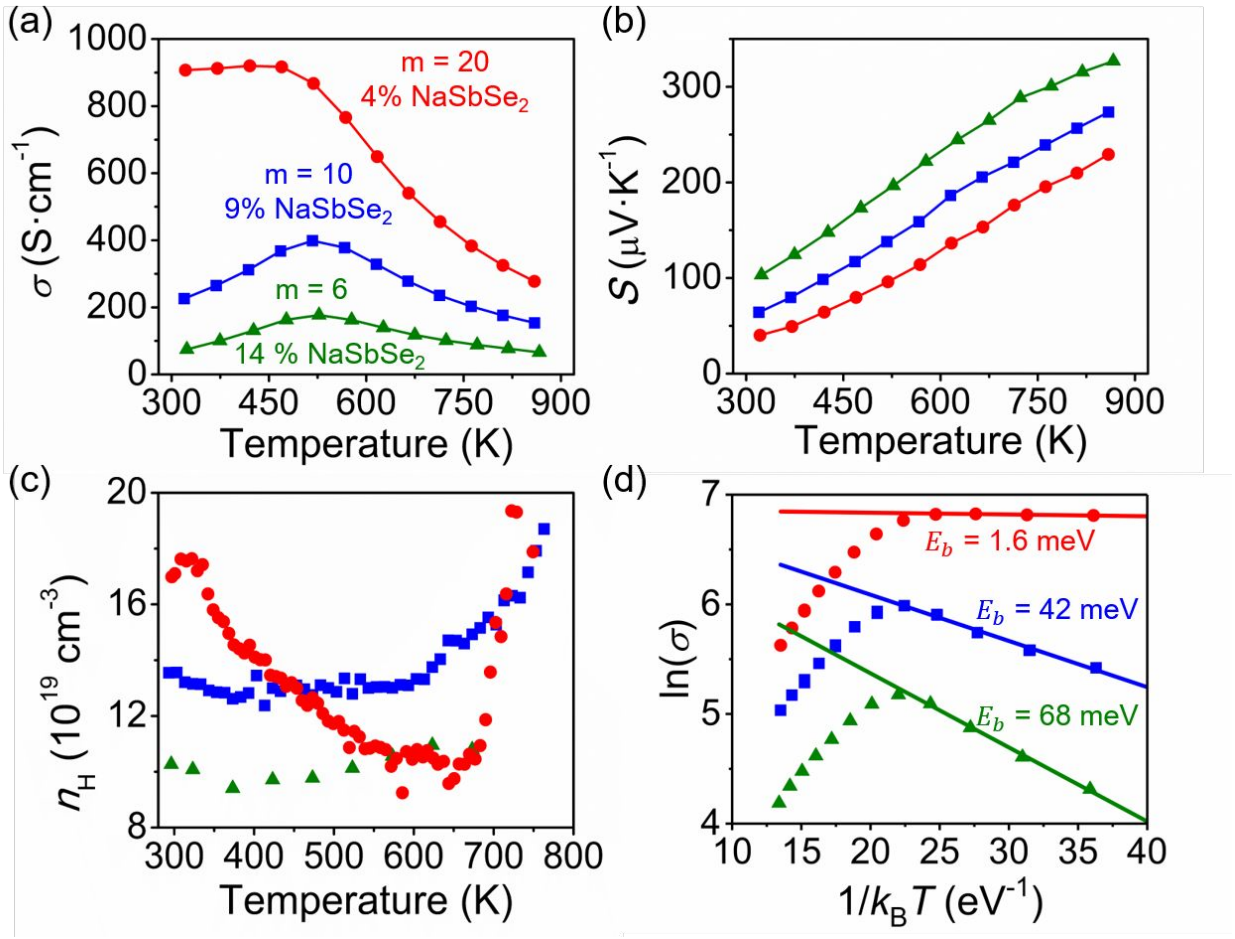

Figure 4: Comparison of the electrical transport properties of comparably doped samples of $NaPb_mSbSe_{m+2}$ for m = 20, 10, and 6 (equivalently ~ 4, 9, and 14 percent $NaSbSe_2$ in PbSe). (a) Electrical conductivities and (b) Seebeck coefficients, (c) variable temperature Hall charge carrier concentrations, and (d) plots of lnσ vs. $1/k_BT$ showing linear temperature dependence over the low T GB dominated regime. The solid lines in (d) show the linear fits used to extract E_b.

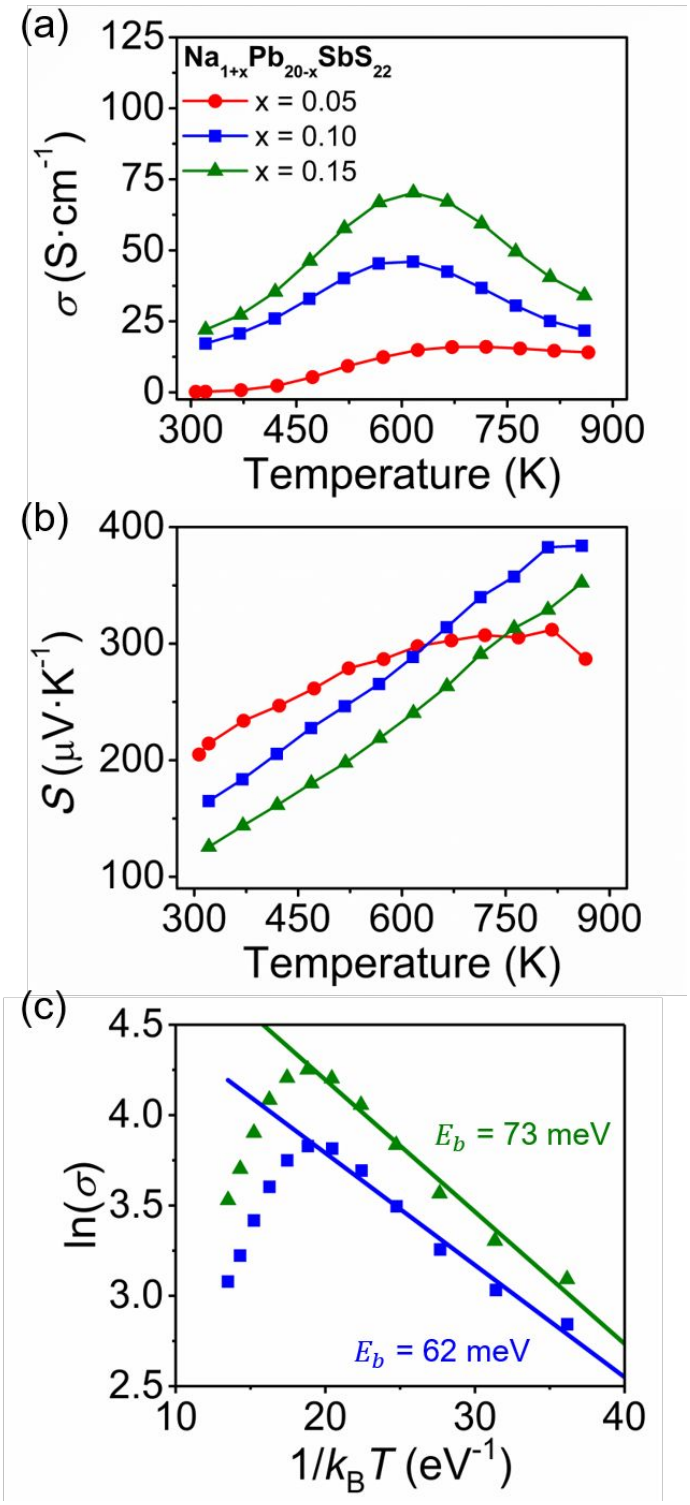

Figure 5: Electrical transport properties of p-type doped m = 20 $NaPb_mSbS_{m+2}$ (nominally $Na_{1+x}Pb_{20-x}SbS_{22}$). (a) Electrical conductivities and (b) Seebeck coefficients (c) plots of lnσ vs. $1/k_BT$ showing linear temperature dependence over the low temperature GB dominated regime. The solid lines in (c) show the linear fits used to extract E_b.

Table 1: DFT calculated relative isotropic dielectric constants for each PbQ and $NaSbQ_2$ (Q = S, Se, Te), as well as Mg_3Sb_2, NbFeSb, TiCoSb, Mg_2Si.

Compound	Calculated ε_r
PbTe	501
PbSe	338
PbS	328
$NaSbTe_2$	58
$NaSbSe_2$	71.8
$NaSbS_2$	113
Mg_3Sb_2	32
NbFeSb	44.7
TiCoSb	32
Mg_2Si	23

TOC figure

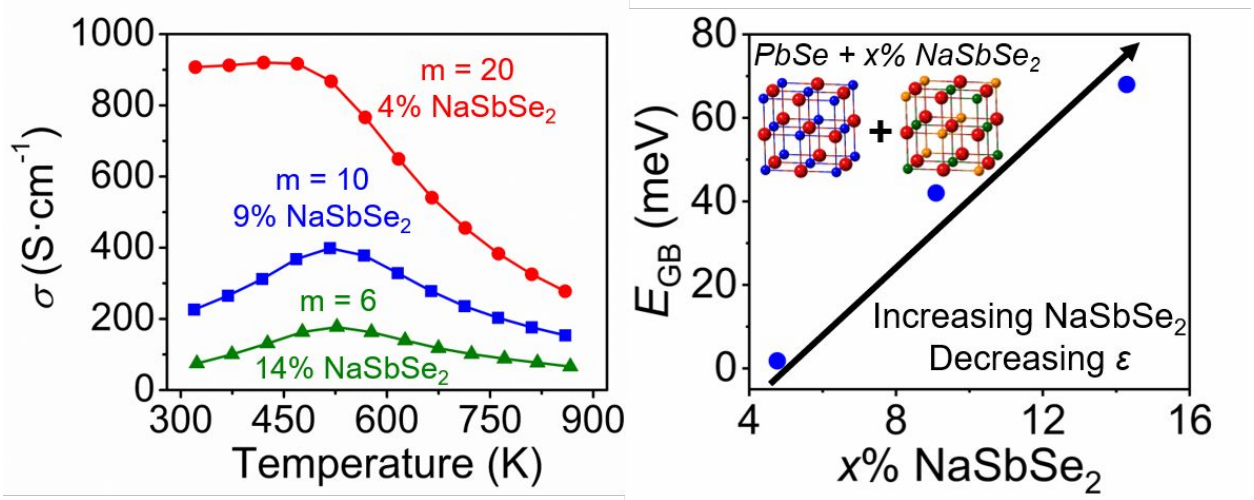

Addressing the irregular electrical conductivity in $PbQ–NaSbQ_2$ thermoelectrics. Increasing the $NaSbSe_2$ fraction weakens charge carrier screening and strengthens GB scattering.

Thermally activated electrical conductivity is increasingly observed in degenerately doped thermoelectric compounds. Such behavior degrades material performance on the cold side and limits device efficiency. While several competing models can qualitatively predict the irregular charge transport, debate remains on the correct microscopic description, and there is likewise little understanding of what materials are most prone to the deleterious behavior. Using the PbQ–$NaSbQ_2$ alloys ($NaPb_mSbQ_{m+2}$) as model systems, we conclusively demonstrate the thermally activated electrical conductivity is due to charge carrier scattering at the grain boundaries (GBs). We furthermore propose simple chemical guidelines for rationalizing and predicting what materials are most vulnerable to GB limited charge transport. We show the magnitude of GB scattering is strongest in compounds that are composed of ionic and weakly polarizable atoms and demonstrate that this simple principle explains the strong GB scattering in numerous otherwise unrelated thermoelectric materials. While small grains are widely believed to be favorable in thermoelectric materials, this work demonstrates how large grains are generally preferred in more ionic semiconductors in order to suppress GB scattering and maintain high charge carrier mobility. This design principle will be broadly applicable to many different thermoelectric materials.